Optimal Design of a Multi-Winding High-Frequency Transformer Using Reluctance Network Modeling (RNM) and Particle Swarm Optimization (PSO) Techniques for the Application of PV-Linked Grid-Connected Modular Multi-Level Inverters

Mohammad Jafari, *Senior Member, IEEE,* Zahra Malekjamshidi, *Member, IEEE* and Md Rabiul Islam, *Senior Member, IEEE*

Abstract- This paper presents an optimal design procedure and development of a multi-winding high-frequency transformer for application in the cascaded modules of a grid-connected modular multi-level Inverter. The transformer should be designed for a certain value of inductances and high efficiency because of its effect on the performance of the entire modular structure. To realize such an accurate design procedure with minimum computation effort and design complexity, a three-stage method including initial design using lumped-parameter modeling, optimal design using particle swarm optimization with reluctance network modeling and finite element method is proposed. An amorphous based toroidal core transformer is designed, developed, and tested under different load conditions and frequency range to validate the design procedure.

Index terms- High-frequency, multi-winding transformer, reluctance network modeling, finite-element, multi-level inverter, particle swarm optimization

I. Introduction

DISTRIBUTED generation has received considerable attention over the past decades as a possible solution for the increasing demand for electrical energy and environmental pollution concerns. In this way, photovoltaic (PV) systems have become more popular due to their availability, simplicity, and lower installation cost compared to the other types of renewable resources [1]. However, the integration of large-scale low-voltage PV power systems into the medium voltage distribution grids in an efficient way has been a challenge and attracted research interest. Modular multi-level inverters (MMIs) have been considered as a solution due to the use of low-rating switching devices in the cascaded conversion modules, which increases the reliability and redundancy of the entire system [2],[3]. Furthermore, high-frequency harmonics of the output voltage and electro-magnetic interference of the system are reduced [4], and smart-grid technologies such as active and reactive power control can be implemented [5]. The MMIs have found different applications in reactive power compensators [6], large scale motor drives [7], and static compensator in ac transmission lines [8]. The basic topology includes multiple cascaded dc-ac conversion modules in each phase of the three-phase system. In the PV-linked MMI, each module consists of a dc-dc converter stage to boost the PV output voltage and maintain the maximum power point tracking (MPPT) followed by the cascaded dc to ac inverter [2]. Dual active bridge (DAB) converter is known as the most promising topology at the dc-dc conversion stage due to the simplicity, high-efficiency, bidirectional power flow, and soft-switching capabilities [9]-[11]. However, a more effective topology can be achieved by connecting more H-bridge cells to a multi-winding high-frequency transformer (MWHFT) as a common magnetic bus to form a multi-active bridge (MAB) converter [13]. This reduces the number of conversion cells and transformers compared to the case of using DAB converters and consequently reduces the size and cost of the entire MMI system due to the modular structure. Among the MAB converter topologies, triple-active bridge (TAB) and quad-active bridge (QAB) converters have found applications in integrating the renewable energy resources using an MWHFT [14]. However, the design of a proper MWHFT with certain specifications for these converters is complicated due to the complexity of structure, high-frequency parasitic effects and non-linear characteristics of the magnetic materials [15], [16]. The classical methods based on the lumped-parameter models (LPMs) rely on many simplifying assumptions that reduce their accuracy [17]. As a result, numerical methods such as finite element method (FEM) have been widely used in more accurate and intricate transformer designs [18]. However, they need extensive computation effort, which makes them unsuitable for iterative optimal design procedures [19], [20]. Furthermore, they need a 2D or 3D model of the electro-magnetic structure with a known dimension prior to analysis, which in most of the designs is not available in the first place. A third method that provides a reasonable design accuracy and computation time is known as reluctance network modeling (RNM) or magnetic equivalent circuit (MEC), which is suitable for iterative design optimization procedures. The method is initially proposed by Laithwait in 1967 [21]. In this method, the magnetic structure is modeled as a network of equivalent electrical elements and is analyzed using classical circuit analysis methods. The

Manuscript received May 9, 2020; revised July 18 and September 15, 2020; and accepted October 2, 2020. This work was supported partially by University of Wollongong, Faculty of Engineering and Information Sciences new staff start up grant.

M. Jafari and Z. Malekjamshidi are with the School of Electrical and Data Engineering, University of Technology Sydney, NSW, Australia.
e-mail:(mohammad.jafari@uts.edu.au; z.malekjamshidi@uts.edu.au)
M.R.Islam is with the School of Electrical, Computer, and Telecommunications Engineering, University of Wollongong (UOW), NSW, Australia.
(e-mail: mrislam@uow.edu.au)

results are then converted to the original magnetic equivalents [13]. It can be used in 2-D and 3D analysis of the magnetic structures [18]. Some of the applications are high-frequency transformer design [14], analysis and design of electrical machines [22] and, their dynamic modeling [23]. Therefore, it is suggested in this paper for iterative analysis of the magnetic structure.

The optimal design of high-frequency transformers using different heuristic methods have been reported in literature. The authors in [24] compared the performance of deterministic and nondeterministic optimization algorithms in global transformer design optimization. Transformer design optimization problem using geometric programming and genetic algorithm also presented in [25] and [26] respectively. However, a magnetic core with a particular shape and dimension is initially availale in these methods or the number of variables and terms in the objective function is limited compared to this paper. On the other hand, particle swarm optimization (PSO) is a metaheuristic method in artificial intelligence that can be used to find approximate solutions for multivariable problems [27]. The method was developed by Eberhart and Kennedy [28], in 1995 and is comparable to genetic algorithms or the ant colony algorithm but is faster and less complicated [29]. It has been used in a wide range of optimization problems in power electronics and power systems, such as the selection of the PI controller [29], reactive power control [30], etc. as reviewed in [31]. The method is used in this paper to find the optimal structure of MWHFT, considering the required specifications and performance. Besides, an optimal transformer design procedure contains the core and copper loss evaluation taking into account the thermal limits. The core loss is conventionally estimated by using the original Steinmetz equation (OSE) in the case of sinusoidal source excitation [32]. Therefore, different modification methods have been proposed in the literature to make it proper for applying to the transformers excited by high-frequency rectangular waveforms [33]. The most common methods are known as modified Steinmetz equation (MSE) [34], natural Steinmetz extension [35], improved generalized Steinmetz equation (IGSE) [36], and the waveform-coefficient Steinmetz equation [37]. Among them, the IGSE method provides better results based on a comparative study presented in [33]. On the other hand, the copper loss can be estimated using either numerical [38] or analytical [39] methods. The numerical methods, such as FEM are accurate but time-consuming. In contrast, analytical methods are mainly based on the imperative and closed-loop equations and determine the copper loss by integrating the losses attributed to each harmonic of the excitation current [14]. In this method, the amplitude of the harmonics is defined using the Furrier transform of the excitation currents. On the other hand, the ac resistance considering skin and proximity effects is usually determined using modified versions of Dowell's equation for loss analysis of the foil and round conductors [40]. At the last stage of design, the resultant core and copper losses as the main sources of temperature are used to create a thermo-electric model of the system and evaluate the magnetic structure for the thermal limit [41].

This paper aims to present a three-stage design procedure for optimal and accurate design of an MWHFT for applications that the transformer performance has a considerable effect on the system performance. In this paper, the transformer is used in a current-fed quad active bridge (CFQAB) converter implemented in each individual module of MMI to integrate the PV outputs. Therefore, it can significantly affect the performance and efficiency of the entire system due to the modular structure. The transformer should be designed optimally considering core and copper losses and also maintains certain values of inductances due to the use of leakage inductances as energy transfer elements in the proposed phase-shift controlled CFQAB converter. Furthermore, similar characteristics for all PV-linked windings is desirable to minimize the cross-coupling effects and circulating power between the ports. To realize such an accurate design with minimum computation effort and design complexity, a three-stage design procedure is proposed in this paper. At first, the dimension of the toroidal core is roughly determined based on the LPM. The resultant dimension then is used as an initial point to determine the exploration domains of the iterative optimal design based on the PSO using RNM due to the capability of providing acceptable accuracy with reasonable computation time. The resultant structure from optimal design is then used to create a 3D model for the third stage based on the FEM to achieve a precise design. The FEM-based design is also used as a reference to measure the accuracy of the LPM and RNM stages. As a complimentary section, core loss, copper loss, and thermal analysis of the designed transformer has been studied briefly. A prototype of the designed transformer is developed using amorphous magnetic materials. An accurate parameter measurement based on the cumulative and differential series-coupling tests, along with the frequency response tests under different load conditions, is conducted to validate the proposed design procedure.

II. Transformer Design Stages

The application of the MWHFT in MMI topology is presented in Fig.1. As can be seen, each phase of the star-connected three-phase system contains multiple cascaded PV-linked converter modules each of them includes a PV-linked CFQAB dc-dc converter followed by a cascaded single-phase dc-ac converter. The CFQAB contains three PV-linked current-fed H-bridges presented as cells 2, 3, and 4, which transfer the PV output powers to a high-voltage side (HVS) bus through cell 1. The transferred power is later converted to a 50 Hz ac voltage by the cascaded dc-ac converter. The MWHFT (consisting of four windings) is used to integrate the PV outputs in the form of a magnetic flux and also isolate the PV ports at the low-voltage side (LVS) from the grid-connected inverter at the HVS. As another application, the MWHFT also is employed in the battery-linked stabilization module to interface a battery to the MMI three-phase legs through a QAB converter. The module increases the flexibility of the active power flow control by bidirectional power flow to/from the battery. According to the discussed applications, the MWHFT has a significant effect on the system's performance due to the modular structure and requires a precise design procedure to achieve the desired specifications. The power flow in the CFQAB converter is controlled by the duty cycle and phase shift variation. As leakage inductances of the transformer windings are used as energy transfer elements in the phase-shift control technique, the windings in LVS (W2, W3, and W4) should present the same leakage inductance and also mutual inductance to the W1 at the HVS. On the other hand, the transformer efficiency considering core and copper loss analysis should be carefully considered in the design

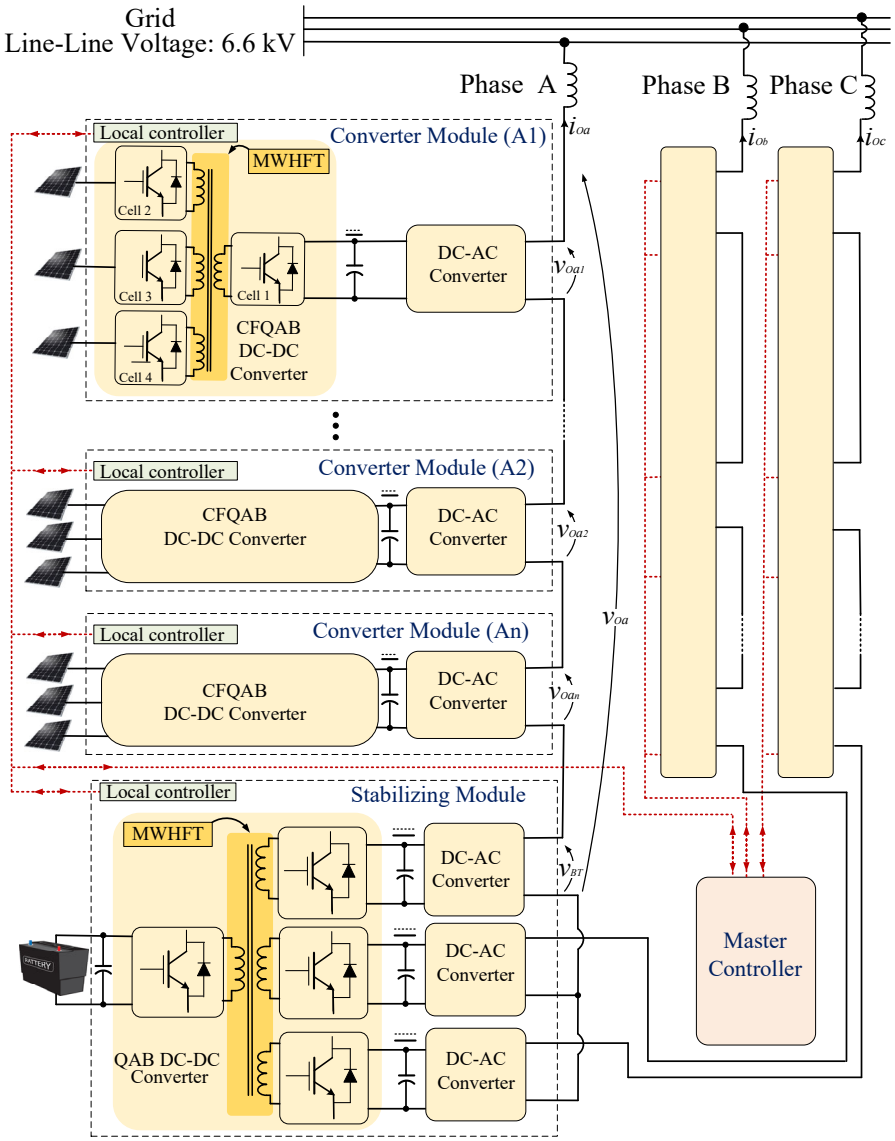

Fig.1. The topology of the proposed MMI and the MWHFT

procedure.

To design the transformer, different magnetic materials have been considered. The soft ferrites present low flux density (0.3-0.5 T), which leads to a larger size transformer and higher core and copper loss. In contrast, Amorphous alloy and Nanocrystalline materials have high saturation flux density, high permeability, and low core loss. However, Nanocrystalline materials have presented lower core loss than the amorphous alloys, although their saturation flux density (0.8–1 T) is much lower than that of amorphous alloys (1.4– 1.6 T) [13]. Finally, the Metglas amorphous alloy (2605SA1) made by Hitachi metals has been selected considering maximum flux density, specific core loss, cost, and flexibility in the design of toroidal cores (available in a strip of 25-mm width and 20-μm thickness). The toroidal shape was selected for the magnetic core in contrast to E and U-shaped cores as it provides more flexibility in the design and development in the lab using thin tapes of Amorphous materials. Furthermore, achieving a symmetrical distribution of windings with similar characteristics for all three conversion cells is possible. The design specifications of the transformer are presented in Table.I and the design procedure is presented in the flowchart of Fig.2. The design procedure is divided into three stages to provide reasonable accuracy and computational effort, as will be reviewed in the following sections.

TABLE.I PARAMETERS OF THE TRANSFORMER

PSO algorithm parameter	Value/ Range
Rated power of Transformer	3600 VA
Rated power of each PV-linked port	1200 VA
Required leakage inductance	L_{l2},L_{l3},L_{l4}: 20 uH, L_{l1}: 15 uH
Specified Mutual inductance	L_{21},L_{31},L_{41}: 50 uH
Switching Frequency	f=10 kHz
Selected magnetic material	Amorphous, 2605SA1
Wire Rated Voltage	V2=V3=V4=110 V, V1=310 V
Rated Current	I1=I2=I3=12 A, I4=12 A
Litz wire strand diameter	27 AWG/ 0.35 mm
The resultant number of turns of windings	N_1:53, N_2, N_3, N_4=18

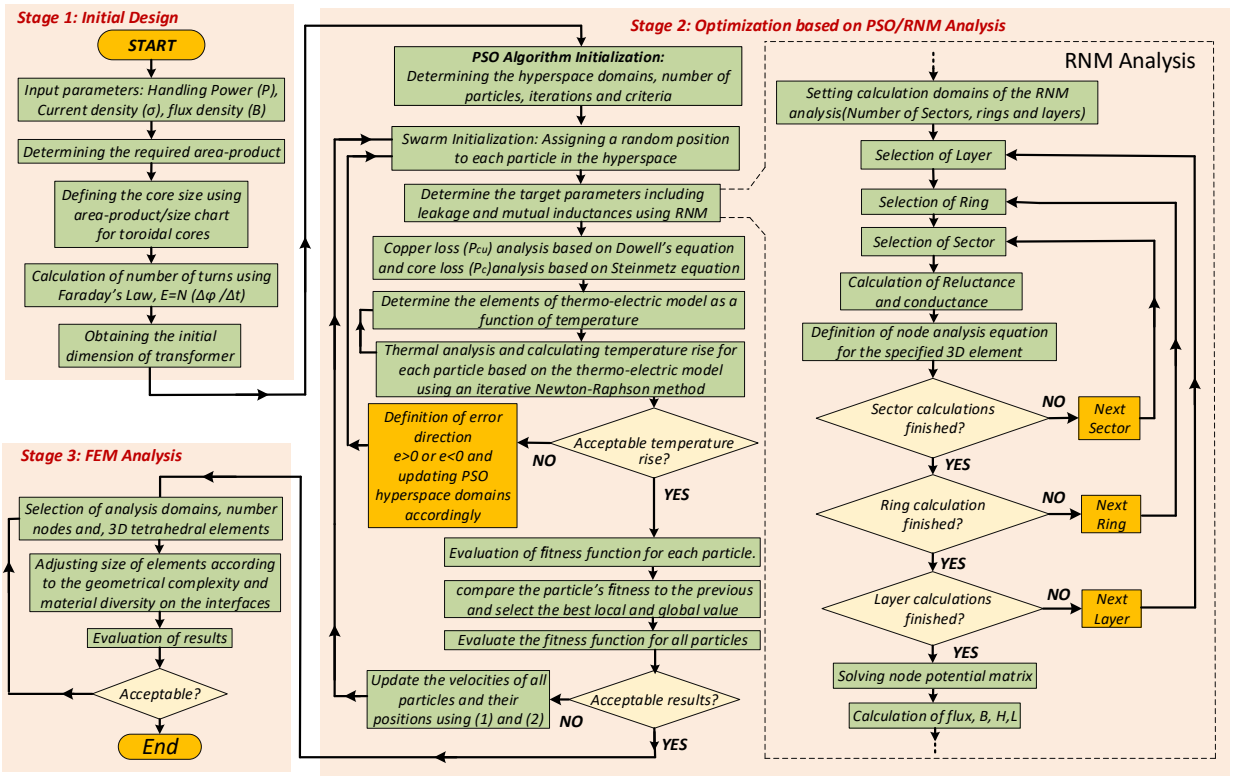

Fig.2 The three-stages design optimization procedure of multi-winding high-frequency transformer

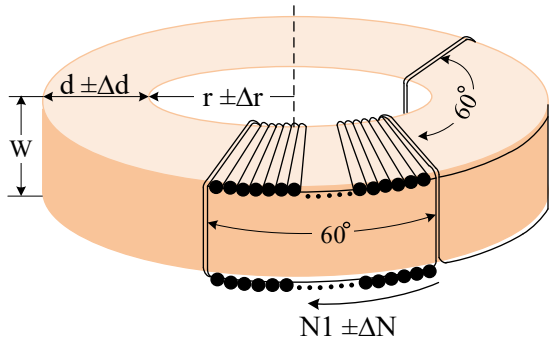

Fig.3 Structure of proposed magnetic core and the design variables

A. Initial Design Based on the Lumped-Parameter Method

The initial design stage is aimed to estimates the core dimension, number of turns and inductances using classical methods of the transformer design by modeling the transformer parameters as lumped elements (known as LPM) [42]. The resultant structure then is used as a reference to determine the proper search domains for the optimization stage and forming the PSO exploration hyperspace. At this stage, to find the initial size of the core, the area-product was defined based on the power handling capacity, current density, and flux density. The resultant value then was used to find the core size from area-product/core-size charts. Finally, the number of turns is calculated using Faraday's law and the value of inductances using provided closed-form equations. The results at this stage are obtained easily but are inaccurate.

B. ptimal Design Based on the RNM Using PSO Algorithm

Due to the iterative nature of optimal design procedures, the RNM method is used at this stage to model the magnetic structure to a network of interconnected equivalent electrical elements, which can be analyzed faster and easier using classical circuit analysis equations. In contrast to the precise numerical methods, the RNM is appropriate for iterative design procedures, does not need to redefine the model of the magnetic core for each iteration, and provides an acceptable accuracy with reasonable computation time [21]. The toroidal core is modeled in the cylindrical coordinate system due to the axial symmetry. The design variables are the internal radius (r), which determines the core window, the core thickness (d), which determines the core cross-section area (due to constant value of W), and the number of turns in the winding one (N_1) and two (N_2) considering (N_2=N_3=N_4) as presented in Fig.3. Therefore, each design point is presented as $(\bar{r}, \bar{d}, \bar{N}_1, \bar{N}_2)$ and attributed to a single particle in the PSO hyperspace and in each iteration, the particle is moved to the new position by adding a differential element $(\pm\Delta r, \pm\Delta d, \text{and } \pm\Delta N)$. Assuming that x_k^i represents the position of particle i at the k-th iteration in the swarm, the updated position then can be presented as:

$$x_{k+1}^i = x_k^i + v_{k+1}^i \qquad (1)$$

where v_{k+1}^i is added as an extra term to move the particle in the exploration space and is determined by

$$v_{k+1}^i = wv_k^i + c_1 r_1 (p_k^i - x_k^i) + c_2 r_2 (p_k^g - x_k^i) \qquad (2)$$

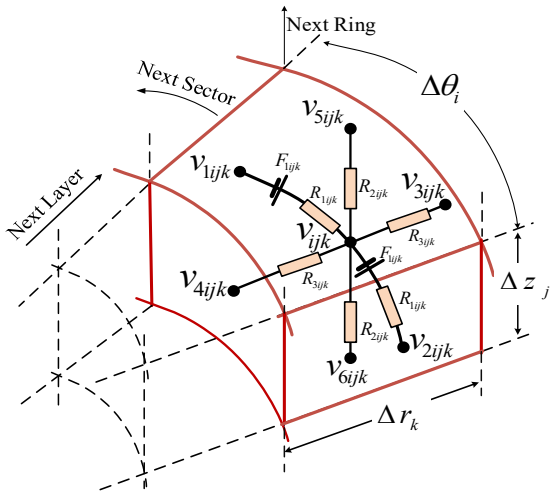

Fig.4 A 3D element for RNM analysis

where the first term of the equation known as inertia factors the tendency of the particle to continue in the same direction it has been moving based on a weighting factor (w) [29], [30]. The second term, known as the cognitive component, provides a linear attraction of the particle towards the best position ever found by the particle in the search space. The third term known as the social component applies a linear attraction towards the best position found by any particle in the swarm [29]. The factors p_k^i and p_k^g are the best individual and the best global particle positions, respectively. Also, c_1 and c_2 are known as the cognitive and social parameters and determine the size of the particle's step towards the best individual and global positions respectively. The amounts of c_1 and c_2 are selected according to the importance of local or global best position and their relative importance can vary from one decision to another. Therefore, the random weights r_1 and r_2 with uniform distribution in the range of [0, 1], are applied to each term. The weighting factor (w) usually decreases linearly during iterations to keep a balance between the local and global explorations and for each iteration k is calculated based on the maximum (w_{max}) and minimum (w_{min}) values from

$$w_k = w_{max} - [(w_{max} - w_{min})/k] \quad (3)$$

For each iteration, the particles' positions are updated, and for each particle, the values of inductances, core loss and copper loss are evaluated using the RNM-based analysis. The resultant values inductances and power loss for each particle are then fitted into the fitness function (4) to be compared to the specified values.

$$f(L, P_{loss}) = \left\{\alpha\left[\sum_{i=1}^{4}\frac{|L_{li}-L_{li}^*|}{L_{li}+L_{li}^*}\right] + \beta\left[\sum_{i=2}^{4}\frac{|L_{i1}-L_{i1}^*|}{L_{i1}+L_{i1}^*}\right] + \gamma\left[\frac{|P_{cu}-P_{cl}|}{P_{cu}+P_c}\right]\right\}, \quad \alpha+\beta+\gamma = 1 \quad (4)$$

where L_{li} and L_{i1} are the leakage inductance of winding i and the mutual inductance of winding i to winding one, P_{cu} and P_c are the copper and core loss of the transformer for the proposed design point related to a particular value of design variables represented by an individual particle position. However, the power density can also be considered as a term in the objective function where the transformer and converter size is a design target. The balance factors α, β, and γ are weighting elements applied to the normalized terms to balance between the importance of design for efficiency and design for specifications. The resultant fitness value is then recorded for each individual particle in the swarm to be used in the next iterations. A similar process is performed for other particles in the swarm hyperspace and the best individual and global fitness positions are recorded. The process then is continued with the next iterations and ended when the fitness function is minimized, and the optimum value of variables is achieved as illustrated briefly in Fig.2. Table.II illustrates the selected parameters of the PSO algorithm.

TABLE.II PARAMETERS OF THE PSO ALGORITHM

PSO algorithm parameter	Value/ Range
Number of selected particles	8
Maximum number of iterations	16
Range of number of turns for W2, W3, and W4	13 – 25 turns
Range of number of turns for W1	45– 68 turns
Range of core thickness (d)	15 – 25 mm
Cognitive and social parameters	c_1=1.85, c_2=2.15
Balance factors α, β and γ	α =0.28, β=0.28, γ=44
Fitness factor range	f_{min} = 0.03, , f_{max} =2.98
Range of weighting	w_{min}=0.4, w_{min} =0.9
Range of core internal radius (r)	25 – 65 mm
Average time of each iteration	105 s
Total computation time	≈28 min

The field analysis based on RNM is performed for each individual particle, and the analysis steps are presented in Fig.2. To do the analysis, the toroidal core area is divided into three different sections, including a free space around the core, magnetic core, and insulator. Assuming operation in the linear section of the magnetization curve, a constant value of permeability is considered in the analysis (this is a reasonable assumption in particular for amorphous 2605SA1 magnetic material due to the linearity of the magnetizing curve). To do the analysis, the entire magnetic structure was divided into thousands of tiny 3D magnetic elements modeled by a network of equivalent electrical circuits. As can be seen in Fig.4, each element presented by Q_{ijk} is formed by a central node linked to the reluctances aligned with the reference axis of a cylindrical coordinate (r, θ, and Z). The indexes i, j, and k represent the unique situation of the 3D element among the entire magnetic structure. Each reluctance is linked to the central node at one side and a node at the boundary surface of the 3D element and is determined based on the geometrical shape and permeability factor of the element. On the other hand, the voltage source F_{ijk}, represents the portion of magnetomotive force (*mmf*) in the corresponding direction and is equal to zero in directions with no magnetic flux. In this particular case, it is almost zero in the r and Z directions. In θ direction, it is determined as a portion of total *mmf* generated by winding depending on the size of the 3D element to the section of the core covered by the winding. The magnetic structure is divided into hundreds of 3D elements which arranged in the sectors in θ, layers in r and, rings in z directions as illustrated in Fig.4. The number of nodes and 3D-elements are determined by the selected number of segments, layers and rings. A network of meshes and grids for the entire toroidal core is achieved considering equivalent electrical elements for each of the elements where the currents in the reluctances represent the

equivalent magnetic flux. Therefore, the currents and equivalent magnetic flux can be determined by applying classical node analysis equations to the network. A set of the equation with the node voltages (v_{ijk}) as unknown variables covering all three analysis areas is achieved and can be written in matrix form as $\acute{Y}\tilde{V} - Y\tilde{F} = 0$ where Y, $\acute{Y}, \tilde{V}$ and $\tilde{F}$ are respectively the central-node-linked conductance, source-linked conductance, central-node voltage, and source voltage matrices [13]. As an initial condition, it is assumed that $v_{ijk} = 0$ for the elements situated on the last layers and rings. The values of the node potentials v_{ijk} is determined by solving the equation using MATLAB and the results can be used to calculate the field intensities (H_i) and the magnetic flux densities (B_i) associated to each element for i =1, 2, ...,6 from

$$H_i = (v_{ijk} - v_i)/l_i \tag{5}$$

$$B_i = \frac{\phi_i}{A_i} \tag{6}$$

where l_i and A_i are the average lengths and cross-section area of the branch, respectively. The closed-form volumetric integration of the distributed stored energy (W_S) enclosed by the volume V can be calculated from

$$W_S = \int_V \frac{H.B}{2} dV = \frac{\mu}{2} \int_V |H|^2 dV \tag{7}$$

where μ is the magnetic permeability [43]. Therefore, the net magnetic energy stored in the i-th branch of the element Q_{ijk} assuming a constant flux density in the element can be calculated from

$$W_i = (\mu V_i H_i^2)/2 \tag{8}$$

where V_i is the volume of the element and is defined as

$$V_i = A_i l_i \tag{9}$$

and the net stored energy of a branch by substituting (5)-(7) into (8) is calculated by

$$W_i = (v_{ijk} - v_{1ijk} - F_i)^2/2R_i \tag{10}$$

where R_i represents the reluctance of the respected branch. The total stored energy of a 3D element Q_{ijk}, then is calculated by integrating the energy in all six branches. Finally, the self-inductance of windings is obtained by assuming a closed surface enclosing the entire magnetic structure and calculating the total enclosed energy (by integrating the energy of all elements inside the surface). The equivalent inductance (L_{eq}) then is estimated from $L_{eq} = (2W_S/I_L^2)$ where W_S is the total enclosed energy and I_L, the current in the winding. On the other hand, the leakage inductances of the windings are estimated, assuming two different enclosed surfaces. One including only the core area and the other enclosed core, insulator and surrounding areas covering the distributed leakage flux. The difference between the stored energies within the two enclosed surfaces then is used to estimate the leakage inductance of each winding. The values of mutual inductances of PV linked windings to winding one (L_{21}, L_{31},and L_{41}) and the leakage inductances (L_{l1}, L_{l2}, L_{l3} and L_{l4}) of all windings of the MWHFT are calculated by using the outlined method. When the magnetic flux density, leakage and mutual inductances are determined, the core and copper loss can be achieved for each individual particle as the third term of the PSO fitness function (4) as detailed below.

C. Core and Copper Loss Analysis

Due to the linear behavior of copper, conduction loss analysis is carried out based on the harmonic contents of the currents in the windings of the transformer [10], [13], [33]. Therefore, the total copper loss in each winding can be calculated by summation of the losses attributed to the main harmonics of the current from

$$P_{Cu} = \sum_{n=1}^{h} P_{Cu,n} \tag{11}$$

where $P_{Cu,n}$ is the resultant copper loss of the n-th harmonic and h the number of harmonics that have considerable effect in the loss analysis. The skin and proximity effects on the winding's resistance can be considered separately for copper loss analysis of each harmonic due to their orthogonality principle [44]. Their effect is modeled as a frequency-dependent resistance for each harmonic in the case of non-sinusoidal currents. Therefore, the resultant loss of the n-th harmonic $P_{Cu,n}$, can be calculated by

$$P_{Cu,n} = \left(\frac{I_n}{\sqrt{2}}\right)^2 R_{ac,n} \tag{12}$$

where $R_{ac,n}$ is the ac resistance of the Litz-wire winding for the n-th harmonic and I_n the peak value of the n-th harmonic of the non-sinusoidal current in the winding. To calculate the copper loss using (11) and (12) for the multi-winding transformer, the equivalent ac resistance, $R_{ac,n}$, and the amplitude of each harmonic, I_n , should be calculated analytically. To find the amplitude of each harmonic of the current in the transformer windings, the cantilever T-model of the transformer should be defined by referring the leakage inductances of windings two, three and four to winding one and neglecting the effect of magnetizing inductance due to small effect on the power transfer [13],[14]. By transforming the model to its equivalent Δ-model and replacing the dc sources plus H-bridge units with the equivalent square wave ac source, the simplified model is achieved as illustrated in Fig.5. To transfer the power from PV-linked LVS to HVS, the voltage at ports two, three and four should be leading to port one by applying phase-shift angles, φ_{21}, φ_{31}, and φ_{41} respectively. Furthermore, a duty cycle (D) is introduced in the PV-linked ports to maintain the MPPT. The amplitude of the dc voltage at the LVS should be varied accordingly to keep a constant volt-second for the windings and maintain the ZVS. The square-wave voltages of the windings presented as v_2, v_3 and v_4 should be written based on their Furrier series for harmonic based analysis in the following general form as

$$v_k(t) = \sum_{n=1}^{\infty} V_{k,n} \sin(n(\omega t + \phi_{k1})) \tag{13}$$

where $V_{k,n}$ for (k=2, 3 and 4) as the amplitude of n-th harmonic of the current in the k-th winding is defined as

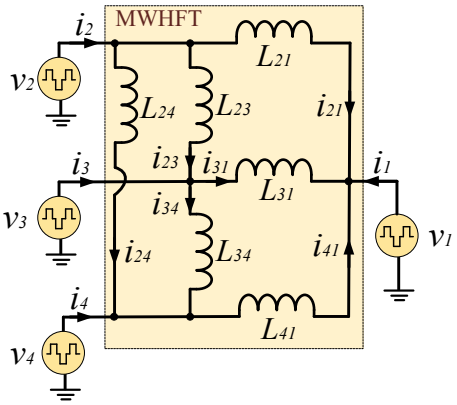

Fig.5 The cantilever model of the MWHFT and supplied square wave voltages sources.

$$V_{k,n} = \frac{2V_{k,min}\,[1-\cos(n\pi)]\cos(n\pi(1-D)/2)}{n\pi D} \tag{14}$$

where $V_{k,min}$ is the minimum value and D the duty cycle of the voltage of the winding. The amplitude of each harmonic of the current in the equivalent inductances presented in the transformer model in Fig.5 is then determined by using their voltage from (14) and the inductance accordingly. The current in each of the windings (i_1, i_2, i_3, and i_4), which is equal to the current supplied by each source, then can be found from node analysis in the equivalent circuit. On the other hand, the ac resistance of each winding attributed to the n-th harmonic ($R_{ac,n}$) should be defined for loss analysis. Considering the skin and proximity effects, the ac resistance of a Litz wire winding is a function of frequency, while the dc resistance (R_{dc}) is relatively constant [38]-[40]. The ratio of $R_{ac,n}$ to R_{dc} known as ac resistance factor, $F_{r,n}$, is defined as $F_{r,n} = R_{ac,n}/R_{dc}$ and is determined based on the Dowell method in this paper. In this method, the round conductors are replaced with the square conductors of the same area, and then an equivalent foil conductor, same as what Dowell analyzed is found. The one-dimensional field analysis is applied to the foil to find the losses [38]-[40]. The equation for the ac resistance factor, $F_{r,n}$, of the m-th layer of a round conductor is

$$F_{r,n} = \zeta_n \left[\upsilon_{1,n} + \frac{2(m^2-1)}{3}\upsilon_{2,n}\right] \tag{15}$$

where

$$\upsilon_{1,n} = \frac{sinh(2\zeta_n)+sin(2\zeta_n)}{cosh(2\zeta_n)-cos(2\zeta_n)} \quad \upsilon_{2,n} = \frac{sinh(\zeta_n)-sin(\zeta_n)}{cosh(\zeta_n)+cos(\zeta_n)} \tag{16}$$

$$\zeta_n = (\frac{\pi}{4})^{0.75}\frac{d}{\delta_n}\sqrt{\eta}\,,\ \eta = \frac{d}{p} \tag{17}$$

η is the porosity factor of the round conductor, d the conductor diameter, and p the distance between centers of two adjacent conductors. The skin depth of round conductor of the n-th harmonic, δ_n, is defined by

$$\delta_n = \sqrt{\frac{\rho_{Cu}}{\pi\mu_0 nf}} \tag{18}$$

where μ_o is the permeability of free space and f the frequency of the waveform. The simplified equation for $\zeta_n \leq 2$ then can be found [38] as

$$F_{r,n} \approx 1 + \frac{(5m^2-1)}{45}\xi_n^4 \tag{19}$$

Using Litz wires in MWHFT implies some modifications to (15) where the number of layers m and the penetration ratio ζ_n are modified effectively to m_l and $\zeta_{str,n}$ from

$$m_l = m\sqrt{n_s} \tag{20}$$

and

$$\zeta_{str,n} = (\frac{\pi}{4})^{0.75}\frac{d_{str}}{\delta_n}\sqrt{\eta_{str}} \tag{21}$$

where η_{str} is the porosity factor of Litz wire [39]. Furthermore, the dependency of dc and ac resistances, and consequently, copper loss to the temperature needs to be considered [45], [46]. The dc and low-frequency resistance R_{dc} is affected by temperature due to the change in the copper resistivity ρ_{Cu} and can be rewritten as

$$R_{dc,T} = R_{dc,T_0}[1 + \alpha^*(T - T_0)] \tag{22}$$

where T_0 is the reference temperature (normally 20 °C), T the actual winding temperature and α^* is the temperature coefficient of resistivity (for copper is 3.93×10^{-3} K^{-1}). On the other hand, the ac resistance R_{ac} is affected by the temperature in a different way due to the variation of both resistivity and penetration ratio. Finally, the ac resistance factor ($F_{r,n}$) for each harmonic content by applying the temperature variation element to the resistivity in (18), (19) and making some arrangement is obtained as

$$F_{r,n,T} = 1 + \frac{F_{r,n,T_0}-1}{[1-\alpha^*(T-T_0)]} \tag{23}$$

where $F_{r,n,T0}$ is the ac resistor factor at the reference temperature T_0 [45]. Therefore, the ac resistance as a function of temperature for n-th harmonic of the current can be found as

$$R_{ac,n,T} = R_{dc,T}F_{r,n,T} = R_{dc,T_0}\left[1 + \alpha^*(T - T_0) + \frac{F_{r,n,T_0}-1}{1+\alpha^*(T-T_0)}\right] \tag{24}$$

More details on the modeling of temperature effects on the estimated copper loss can be found in [45], [46]. Numerical simulations based on the above-mentioned method shows that the copper loss in each of the windings depends on the duty cycle of current (D) and the phase-shift of its voltage respected to the other windings. As presented in Fig.6, when φ_{41} is changing from 0 to π/2, the copper loss is minimized when φ_{41}=0.5*φ_{31}=0.5*φ_{21} for the whole range of φ_{21} and φ_{31}. The reason is that φ_{41} is leading to W1 and also lagging to W2 and W3 with the same phase angle. Therefore, the winding is sending power to W1 and also receiving power from W2 and W3 simultaneously. As a result, the net power transfer and consequently, current and copper loss is minimized at this point. The 3D graph in Fig.7 shows the effect of the duty cycle on the copper loss. As can be seen, for all cases of $\varphi_{21}$and φ_{31}, the copper loss increases in the winding four by reducing the duty cycle of excitation voltage.

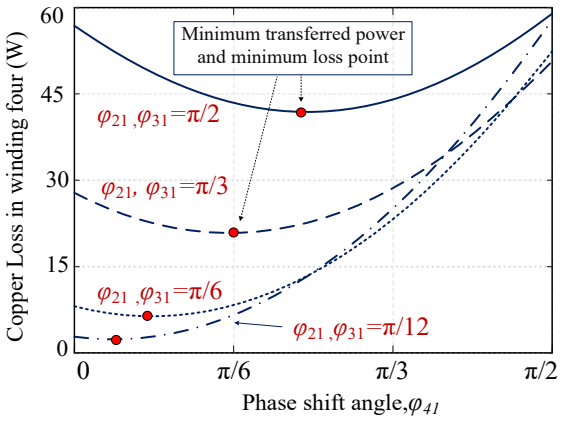

Fig.6 The copper loss of the winding four of MWHFT as a function of phase shift angles φ_{21}, φ_{31}, and φ_{41}.

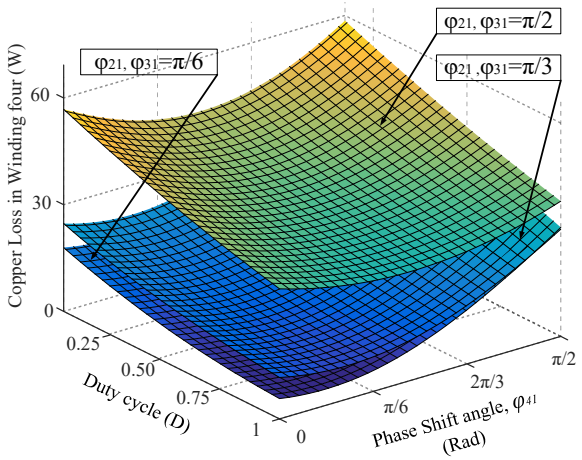

Fig.7 (a) The copper loss of MWHFT as a function of phase shift angle (φ) and duty cycle (D).

The reason is that smaller duty cycles happen at the higher amplitudes of excitation voltage, which increases the amplitude of the main harmonics of the current in the winding (especially first harmonic). On the other hand, the core loss resistance for the resultant structure is determined by using the Steinmetz equation based on the flux density and frequency [47]. In this paper, the original Steinmetz equation is modified for the square-wave excitation as presented below and is detailed in [35], [38].

$$P_c = 2^{n+m} k_i f^m B_{max}^n D^{n-m+1} \quad (25)$$

where B_{max} is the maximum flux density in the case of rectangular excitation voltage, k_i is the modified value of k, and D is the duty cycle of the applied waveform. The values of constant coefficients m, n, and k_i have been determined roughly based on the experimental measurements reported in [13] for amorphous alloy 2605SA1. The core and copper losses resulted at this stage are then used to determine the temperature rise in the transformer using a thermo-electric model of the transformer based on the method presented in [47]. The model is developed considering the heat transfer mechanisms of conduction, convection and radiation where the winding and the magnetic core are modeled as heat sources of the system. The temperature rise in windings and the magnetic core as the main heat sources because of the

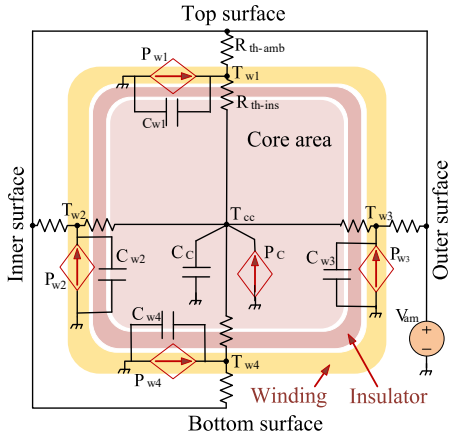

Fig.8 The thermo-electric model of the magnetic core

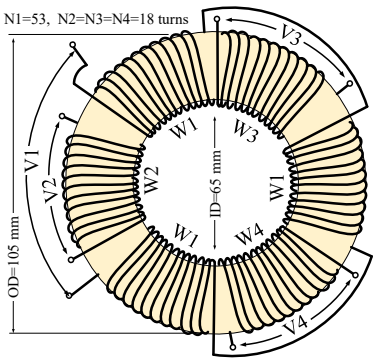

Fig.9 Structure and the dimension of the optimally designed transformer

copper and core losses are modeled by the current sources. Once all components of the equivalent thermo-electric model are defined, the energy balance equations are used to determine the temperature of selected hot points on the surface. Furthermore, the insulation layers are modeled as thermal resistors due to the poor thermal conductivity, as presented in Fig.8. An iterative solution based on the Newton-Raphson method is employed to solve the equations due to the dependency of the model parameters on the temperature, as is detailed in [43], [48]. In this paper, a maximum temperature rise of ΔT=40ºC with ambient temperature (T_{amb}= 30ºC) is considered as the thermal limit for both windings and the magnetic core. If the temperature rise of the particle exceeds the limit, the result is not accepted and the PSO searching domain is modified accordingly. The resultant values of core and copper loss for the particle then is fitted into the fitness function (4). Similar RNM field analysis and core and copper loss analysis and fitness function evaluation are performed for other particles of the swarm in each iteration. When a majority of particles reached the same result and a desirable design which minimized the fitness function is achieved, the resultant structure is selected as the optimal design. Fig.9 shows the dimension of the optimally designed transformer. As can be seen, winding one (W1) is divided into three sections distributed around the magnetic core symmetrically. The windings of the PV-linked conversion cells (W2, W3, and W4) have a similar number of turns (N_1:53, N_2, N_3, N_4=18), winding length and physical

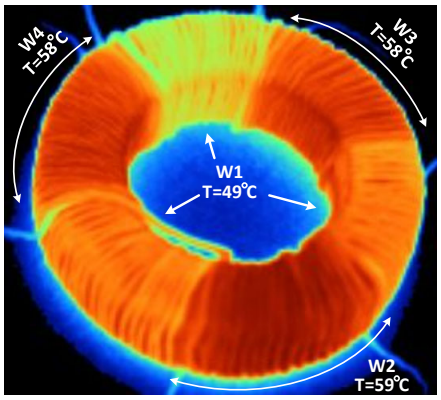

(a)

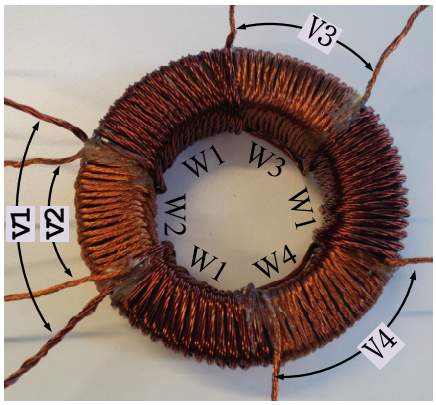

(b)

Fig.10 (a), the experimentally developed multi-winding transformer and (b), the experimentally measured temperature

situation respected to W1 to present similar leakage and mutual inductances. The internal and external diameter of the core is obtained as 65 and 105 mm respectively with a fixed thickness of 25mm. The experimentally developed transformer using Amorphous materials is presented in Fig.10 (a). The Litz wires have been used to reduce the skin and proximity effects due to the high-frequency currents [14],[46]. The proposed thermo-electric model predicted a temperature rise of ΔT=26 ºC ($Tmax$=56 ºC) under the full load excitation currents supplied to the windings. However, in the experimental test, the measured temperature of the developed transformer in full load in steady-state condition was about 58 ºC, as presented in Fig.10 (b). The measured temperature was slightly more than predicted but still in the acceptable range.

D. Precise Design Using Finite Element Method

The last stage of design is analyzing the resultant structure using FEM to perform a more accurate analysis of magnetic field distribution and evaluation of inductances. The results also can be used as a criterion to find out the accuracy of previous stages. As FEM needs a predefined 3D model of the magnetic core for the field analysis, the resultant structure of the prior stage can be used. The magnetic structure is analyzed using ANSYS Maxwell with adaptive mesh generation. A 3D CAD model of the transformer based on the results of the previous stage is developed and is meshed into about 24300 tetrahedral

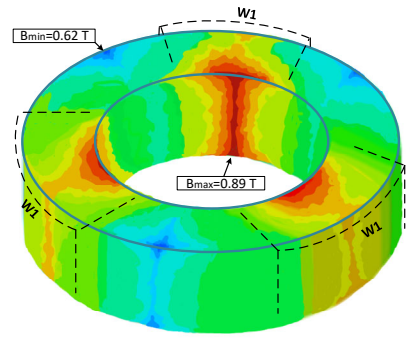

Fig.11 FEM analysis of magnetic flux distribution in the magnetic core when only winding one is exited.

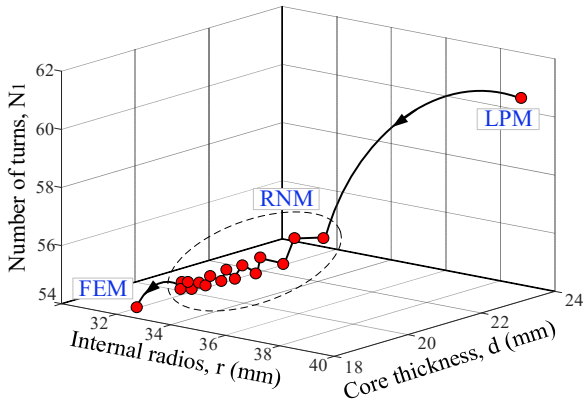

Fig.12 The transition path of the three-stage design procedure

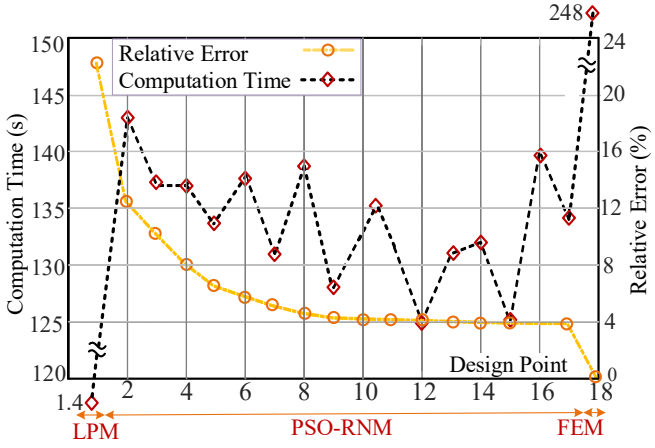

Fig.13 The experimental set of the proposed MMI and the MWHFT

elements. The boundary and initial conditions of the analysis are set according to the proposed application, and proper solvers are selected. Fig.11 shows the flux distribution associated with W1 in the magnetic core based on the FEM analysis. Fig.12 illustrates the transition of the design procedure between the design points according to the design variables. Fig.13 presents the computation time of the design stages LPM, PSO-RNM, and FEM and also the relative error compared to the FEM case as a reference to contrast the accuracy. The LPM results presented 22.4% error with 1.4s computation time, the PSO-RNM error reduced from

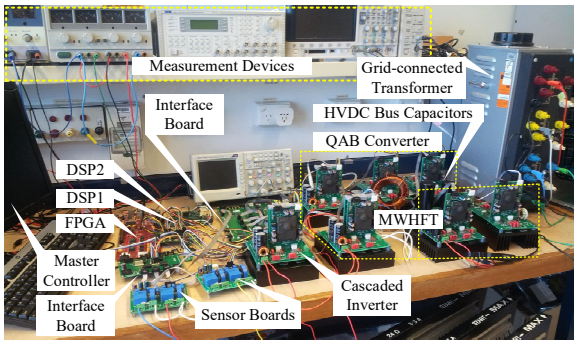

Fig.14 The experimental set of the proposed MMI and the MWHFT

17.57% to 3.91% with the average time of 134s for each iteration and a total time of 34 min. The FEM as the reference method, presented the most accurate result for 248s. The entire design procedure took about 38 min which is less than using FEM-based optimization and also doesn't need a pre-design 3D model of the transformer, which is not available in the first place due to the presence of multiple design variables. A pareto-front of non-dominated design by changing the weighting factors of α, β and γ in the objective function and running the optimization process derived to show that the optimization process is a trade-off among the multiple design objectives. It was seen that considering only inductances as the dominant element in the optimization process (by selecting α=β=0.49 and γ= 0.02), resulted in a slightly higher values for inductances with a small average error (3.5%) but increased the normalized error between the core and copper losses to about 28% (higher copper loss). On the other hand, considering the efficiency as the dominant factor (by selecting α=β=0.01 and γ=0.98) resulted in an almost equal values of the core and copper loss but 16% less than the multi-objective case. The value of inductances is also reduced by 13% in average for both leakage and mutual inductances.

III. Experimental Validation

The designed transformer is used in a prototyped MMI system, as presented in Fig.14. To validate the design procedure of the MWHFT, the transformer parameters are measured as a function of excitation current and excitation frequency and have been compared to the numerically calculated values. The test procedure contained conventional open-circuit tests where the secondary is open-circuited with the test voltage applied to the primary and also in reverse direction where the primary is open-circuited. In the case of the short circuit test, series coupling differentially and cumulatively connected tests are used as presented in Fig.15 due to their accuracy compared to the conventional short-circuit test. The measured real and imaginary parts of the measured impedance in the differentially and cumulatively coupled tests (referring to Fig.15) is obtained as:

$$Z_i(diff) = R_{13}(diff) + j\omega L_{13}(diff) = [R_{W1} + R_{W3} + (1-n)^2 R_m] + j\omega[L_{l1} + L_{l3} + (1-n)^2 L_{13}] \quad (26)$$

$$Z_i(cum) = R_{13}(cum) + j\omega L_{13}(cum) = [R_{W1} + R_{W3} + (1+n)^2 R_m] + j\omega[L_{l1} + L_{l3} + (1+n)^2 L_{13}] \quad (27)$$

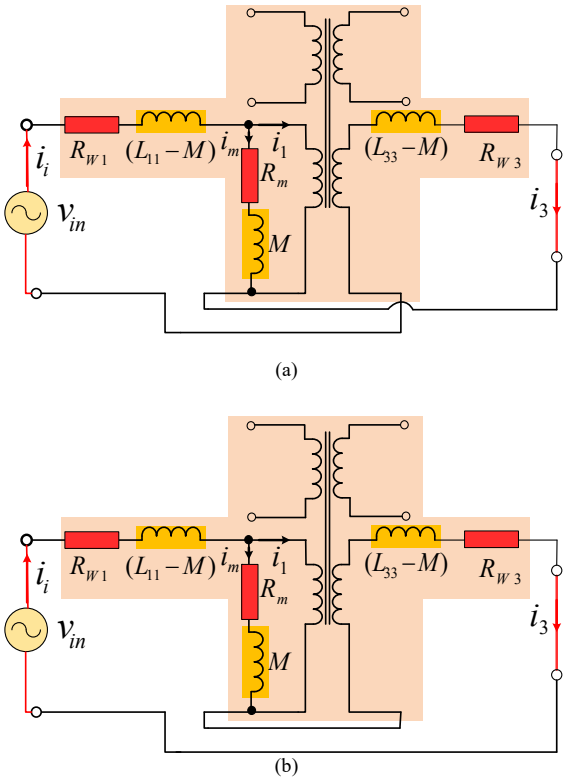

Fig.15 The series coupling test techniques for measuring transformer parameters, (a) differentially and, (b) cumulatively connected

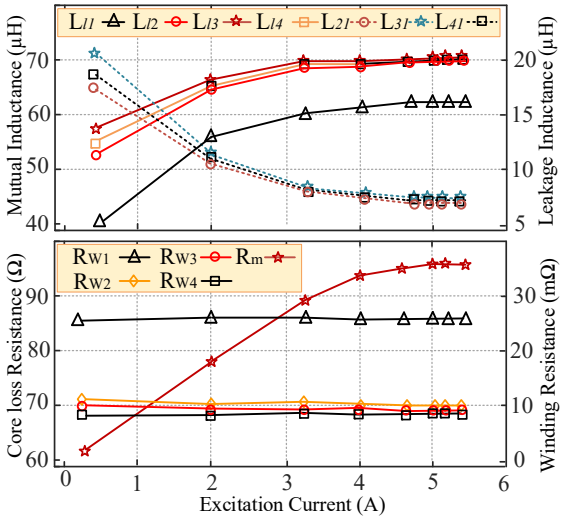

Fig.16 The experimentally measured parameters of the designed transformer as a function of excitation current.

The test procedure has also been conducted on the other pairs of windings in a similar way. Solving the resultant equation in the open and short-circuit tests, results in the transformer parameters, as is explained in detail in [13], [48]. Fig.16 illustrates the inductances and resistances of windings as a function of excitation current. As can be seen, the winding resistance is independent of excitation current, while the equivalent core loss resistance is increasing with the current. On the other hand, the leakage inductance of the windings increases and the mutual inductance decreases with an increase in the excitation current. Comparing the

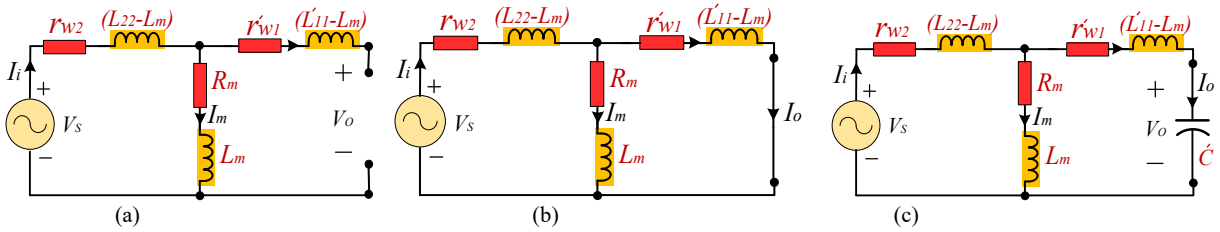

Fig.17 Experimental test of MWHFT for (a) open circuit (b) short circuit and, (c) capacitive load conditions

results for the rated current of 5A in PV-linked windings (W2, W3 and W4) with the design specifications presented in Table.I, shows an average error of less than 6%.

In the next stage, the frequency response of the experimentally developed transformer is compared to the numerically obtained parameters for three cases of open circuit, short circuit and capacitive load. The test is going to indicate the accuracy of the designed and experimentally measured parameters for a wide range of frequency due to the harmonic-based nature of supplied currents and voltages. Furthermore, the difference between the characteristics of the windings (W2, W3, and W4) for a wide range of frequency and also their adaptation to the numerically obtained results is studied. The excitation voltage with variable frequency was applied to winding two, three, and four, and the output signal is collected from winding one. The magnetizing inductance and the equivalent core loss resistance are replaced by their corresponding series elements, as presented in Fig.17 [32], [33]. The output to the input transfer function in the case of the open-circuit test [referring to Fig.17 (a)] when excitation voltage is applied to W2 and output voltage collected from W1 can be written as

$$\frac{V_O}{V_S} = \frac{R_m + SL_m}{r_{W1} + R_m + SL_{22}} \tag{28}$$

and in the case of the short circuit [Fig.17 (b)] as

$$\frac{I_O}{V_S} = \frac{Z}{[r_{W2} + (L_{22} - L_m)S + Z][r'_{W1} + (L'_{11} - L_m)S]}$$

$$[Z]^{-1} = [R_m + SL_m]^{-1} + [r'_{W1} + S(L'_{11} - L_m)]^{-1} \tag{29}$$

In the case of capacitive load [Fig.17 (c)], the transfer function can be written as

$$\frac{V_O}{V_S} \frac{Z}{[r_{W2} + (L_{22} - L_m)S + Z][1 + SC'r'_{W1} + S^2C'(L'_{11} - L_m)]}$$

$$[Z]^{-1} = [R_m + SL_m]^{-1} + [r'_{W1} + S(L'_{11} - L_m) + 1/SC']^{-1} \tag{30}$$

As can be seen in Fig.18, the frequency response of the prototype transformer for all three windings adapts to the numerically calculated model. Furthermore, all three windings presented the same frequency response to winding one due to their symmetrical structure and similar characteristics. The frequency range of 10kHz to 100 kHz includes the switching frequency (f=10 kHz) and, 1st, 2nd, 3rd, …, and 5th harmonics of the voltage and current waveforms to properly models the actual operating

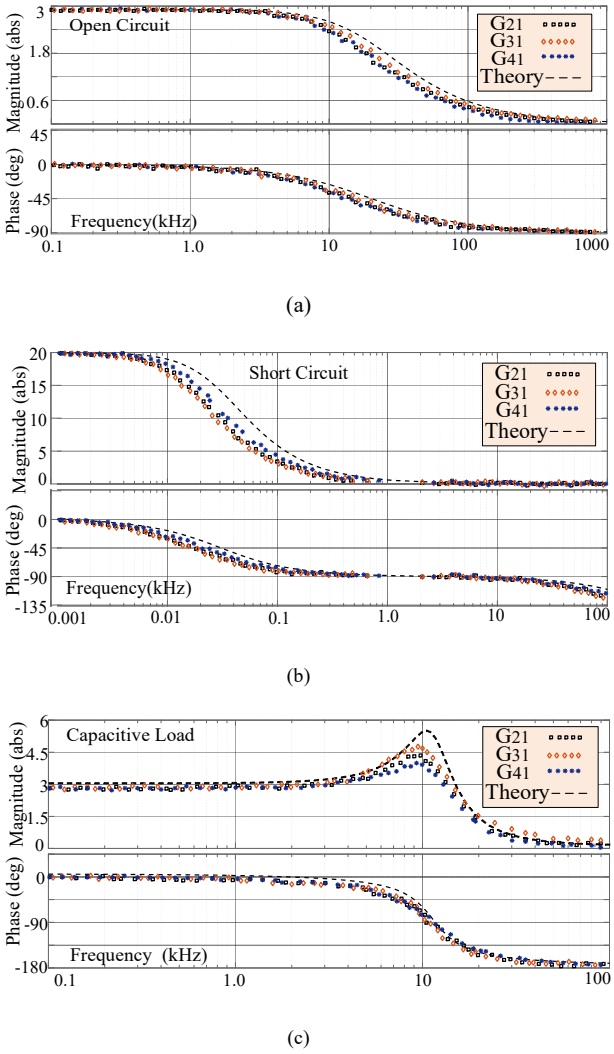

Fig.18 Comparison of the experimentally measured and numerically calculated frequency response of the MWHF for (a) open-circuit test, (b) short circuit test and (c) capacitive load

condition of MWHFT when the phase-shifted square wave voltages are applied to the windings.

To validate the performance of the optimal design procedure regarding the efficiency, as the second term of objective function, a loss breakdown of a converter is presented in Fig.19. The power losses are measured for three operating points including maximum (3.6 kW), nominal (2.7 kW) and light load (1.1 kW) conditions. The value of each loss can be seen on the vertical axis and also as a percentage of total measured loss in the related load condition.

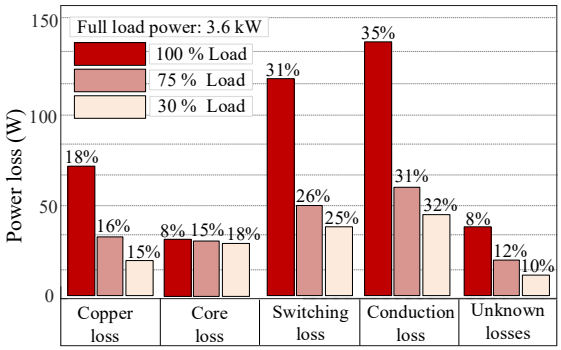

Fig.19 The loss breakdown of a converter module under full load, nominal and light load conditions. Each item is presented as a percentage of total measured loss.

The transformer loss including core and copper losses, switching loss and conduction loss are measured based on the method presented in [14], [49]. The measurments show that the transformer loss account for approximately 30% of total loss. The core loss remains almost the same for all operating conditions and is close to the copper loss for the nominal operating range as a result of optimal design for this condition. The maximum efficiency of the converter is measured at the nominal load equal to 91.5% and for maximum and light load conditions as 89% and 86.5%, respectively.

IV. Conclusion

In this paper, an optimal design procedure for a multi-winding high-frequency toroidal transformer for application in a PV-linked modular multi-level inverter is presented. The transformer was designed for a particular value of inductances and optimal efficiency using the LPM as the initial stage, PSO-based RNM as an optimal iterative stage, and the FEM as a precise design stage. In contrast to the FEM as a reference, the LPM results presented 22.4% error with 1.4s computation time, RNM error starts from 12.57% for the best global result in the swarm in the first iteration of PSO algorithm and reduced to 3.91% with the average time of 105s for each iteration. The FEM, as the most accurate result, took 224s for running. Comparing measured and numerically simulated parameters of the transformer showed a maximum error of less than 6%, which validated the design procedure.

References

[1] Bimal K. Bose, "Photovoltaic Energy Systems," *Power Electronics in Renewable Energy Systems and Smart Grid: Technology and Applications*, IEEE, 2019, pp.347-389

[2] Y. Shi, R. Li, Y. Xue and H. Li, "High-Frequency-Link-Based Grid-Tied PV System With Small DC-Link Capacitor and Low-Frequency Ripple-Free Maximum Power Point Tracking," *IEEE Trans. Power Electron.,* vol. 31, no. 1,pp. 328-339, Jan. 2016.

[3] L. F. Costa, F. Hoffmann, G. Buticchi and M. Liserre, "Comparative Analysis of Multiple Active Bridge Converters Configurations in Modular Smart Transformer," *IEEE Trans. Ind. Electron.,* vol. 66, no. 1, pp. 191-202, Jan. 2019.

[4] L. Liu, H. Li, Y. Xue and W. Liu, "Decoupled Active and Reactive Power Control for Large-Scale Grid-Connected Photovoltaic Systems Using Cascaded Modular Multilevel Converters," *IEEE Trans. Power Electron.*, vol. 30, no. 1, pp. 176-187, Jan. 2015.

[5] L. Liu, H. Li, Y. Xue and W. Liu, "Reactive Power Compensation and Optimization Strategy for Grid-Interactive Cascaded Photovoltaic Systems," *IEEE Trans. Power Electron.*, vol. 30, no. 1, pp. 188-202, Jan. 2015.

[6] Jin Wang and F. Z. Peng, "Unified power flow controller using the cascade multilevel inverter," *IEEE Trans. Power Electron*., vol. 19, no. 4, pp. 1077-1084, July 2004.

[7] M. Hagiwara, K. Nishimura, H. Akagi, "A medium-voltage motor drive with a modular multilevel PWM inverter," *IEEE Trans. Power Electron*., vol. 25, no. 7, pp. 1786-1799, Jul. 2010.

[8] K. Sano, M. Takasaki, "A transformerless D-STATCOM based on a multivoltage cascaded converter requiring no dc source" *IEEE Trans. Power Electron.,* vol. 27, no. 6, pp. 2783-2795, Jun. 2012.

[9] M. Jafari, Z. Malekjamshidi, J. Zhu and M. Khooban, "A Novel Predictive Fuzzy Logic-Based Energy Management System for Grid-Connected and Off-Grid Operation of Residential Smart Microgrids," *IEEE Journal of Emerg.Selected Topics in Power Electron.*, vol. 8, no. 2, pp. 1391-1404, June 2020.

[10] M. Jafari, Z. Malekjamshidi, D. D. Lu and J. Zhu, , "Development of a Fuzzy-Logic-Based Energy Management System for a Multiport Multioperation Mode Residential Smart Microgrid," *IEEE Trans. Power Electron.*, vol. 34, no. 4, pp. 3283-3301, April 2019.

[11] M.Jafari, Z.Malekjamshidi, and J.G.Zhu, "A magnetically coupled multi-port, multi-operation-mode micro-grid with a predictive dynamic programming-based energy management for residential applications," *International Journal of Electrical Power & Energy Systems*, vol. 104, pp. 784-796, January 2019.

[12] M.Jafari and Z.Malekjamshidi, "Optimal energy management of a residential-based hybrid renewable energy system using rule-based real-time control and 2D dynamic programming optimization method," *Renewable Energy*, vol. 146, pp. 254-266, 2020.

[13] L. F. Costa, F. Hoffmann, G. Buticchi and M. Liserre, "Comparative Analysis of Multiple Active Bridge Converters Configurations in Modular Smart Transformer," *IEEE Trans. Ind. Electron.*, vol. 66, no. 1, pp. 191-202, Jan. 2019.

[14] L. F. Costa, G. Buticchi and M. Liserre, "Quad-Active-Bridge DC–DC Converter as Cross-Link for Medium-Voltage Modular Inverters," *IEEE Trans. Ind. Appl.*vol. 53, no. 2, pp. 1243-1253, March-April 2017.

[15] M. Jafari, Z. Malekjamshidi, G. Lei, T. Wang, G. Platt and J. Zhu, "Design and Implementation of an Amorphous High-Frequency Transformer Coupling Multiple Converters in a Smart Microgrid," *IEEE Trans. Ind. Electron.*, vol. 64, no. 2, pp. 1028-1037, Feb. 2017.

[16] M. Jafari, Z. Malekjamshidi and J. Zhu, "Copper Loss Analysis of a Multiwinding High-Frequency Transformer for a Magnetically-Coupled Residential Microgrid," *IEEE Trans. Ind. App.* vol. 55, no. 1, pp. 283-297, Jan.-Feb. 2019.

[17] Hamdi ES. Design of small electrical machines. Chichester, U.K.: Wiley; 1998.

[18] B. Auchmann, B. Flemisch, and S. Kurz, "A discrete 2-D formulation for 3-D field problems with continuous symmetry," *IEEE Trans. Magn.,* vol. 46, no. 8, pp. 3508–3511, Aug. 2010.

[19] T. W. Preston and J. P. Sturgess, "Implementation of the finite-element method into machine design procedures," in *Proc. Int. Conf. Electr.Mach.Drives*, 1993, pp. 312–317.

[20] S. R. H. Hoole, A. Mascrenghe, K. Navukkarasu, and K. A. S. K. Sivasubramaniam, "An expert design environment for electrical devices and its engineering assistant," *IEEE Trans. Magnetics.*, vol. 39, no. 3, pp. 1693–1696, May 2003.

[21] E. R. Laithwaite, "Magnetic equivalent circuits for electrical machines," in *Proc. Inst. Electr. Eng.*, vol. 114, no. 11, pp. 1805–1809, Nov. 1967.

[22] H. Gorginpour, H. Oraee and R. A. McMahon, “A Novel Modeling Approach for Design Studies of Brushless Doubly Fed Induction Generator Based on Magnetic Equivalent Circuit,” *IEEE Trans. Energy Conversion*, vol. 28, no. 4, pp. 902-912, Dec. 2013.

[23] R. Wang, S. Pekarek, M. L. Bash, A. Larson and R. V. Maaren, “Incorporating Dynamics in a Mesh-Based Magnetic Equivalent Circuit Model of Synchronous Machines,” *IEEE Trans. Energy Conversion*, vol. 30, no. 3, pp. 821-832, Sept. 2015.

[24] E. I. Amoiralis, M. A. Tsili, D. G. Paparigas and A. G. Kladas, "Global Transformer Design Optimization Using Deterministic and Nondeterministic Algorithms," *IEEE Trans. on Ind.Appl.*, vol. 50, no. 1, pp. 383-394, Jan.-Feb. 2014, doi: 10.1109/TIA.2013.2288417.

[25] R. A. Jabr, "Application of geometric programming to transformer design," *IEEE Trans. Magnetics*, vol. 41, no. 11, pp. 4261-4269, Nov. 2005, doi: 10.1109/TMAG.2005.856921

[26] P. Shuai and J. Biela, "Design and optimization of medium frequency, medium voltage transformers," *2013 15th European Conference on Power Electronics and Applications (EPE)*, Lille, 2013, pp. 1-10, doi: 10.1109/EPE.2013.6634423.

[27] G. Torres and V. Quintana, “On a nonlinear multiple-centrality-corrections interior-point method for optimal power flow,” *IEEE Trans. Power Syst*., vol. 16, no. 2, pp. 222–228, May 2001.

[28] J. Kennedy and R. Eberhart, “Particle swarm optimization,” in Proc. *IEEE Int. Conf. Neural Netw. (ICNN),* Nov. 1995, vol. 4, pp. 1942–1948.

[29] S. S. Sebtahmadi, H. B. Azad, S. H. A. Kaboli, M. D. Islam and S. Mekhilef, “A PSO-DQ Current Control Scheme for Performance Enhancement of Z-Source Matrix Converter to Drive IM Fed by Abnormal Voltage,” *IEEE Trans. Power Electron.*, vol. 33, no. 2, pp. 1666-1681, Feb. 2018, doi: 10.1109/TPEL.2017.2679118.

[30] W. Zhang, Y. Liu, and M. Clerc, “An adaptive PSO algorithm for reactive power optimization,” in Proc. 6th Int. Conf. Advances in Power SystemControl,OperationandManagement,Nov.2003,pp.302–307.

[31] Y. del Valle, G. K. Venayagamoorthy, S. Mohagheghi, J. Hernandez and R. G. Harley, “Particle Swarm Optimization: Basic Concepts, Variants and Applications in Power Systems,” *IEEE Trans. Evolutionary Computation*, vol. 12, no. 2, pp. 171-195, April 2008, doi: 10.1109/TEVC.2007.896686.

[32] C. P. Steinmetz, “On the law of hysteresis,” *AIEE Trans.*, vol. 9, pp. 3-64, Sep. 1892.

[33] I. Villar, U. Viscarret, I. Etxeberria-Otadui and A. Rufer, “Global Loss Evaluation Methods for Nonsinusoidally Fed Medium-Frequency Power Transformers,” *IEEE Trans. Ind. Electron.*, vol. 56, no. 10, pp. 4132-4140, Oct. 2009.

[34] J. Reinert, A. Brockmeyer and R. W. A. A. De Doncker, "Calculation of losses in ferro- and ferrimagnetic materials based on the modified Steinmetz equation," in *IEEE Transactions on Industry Applications*, vol. 37, no. 4, pp. 1055-1061, July-Aug. 2001, doi: 10.1109/28.936396.

[35] A. Van den Bossche, V. C. Valchev, and G. B. Georgiev, “Measurement and loss model of ferrites with non-sinusoidal waveforms,” in *Proc. 35th Annu. IEEE PESC*, Jun. 20–25, 2004, vol. 6, pp. 4814–4818.

[36] K. Venkatachalam, C. R. Sullivan, T. Abdallah, and H. Tacca, “Accurate prediction of ferrite cores loss with nonsinusoidal waveforms using only Steinmetz parameters,” in *Proc. IEEE Workshop Comput. Power Electron.*, Jun. 3–4, 2002, pp. 36–41.

[37] W. Shen, “Design of high-density transformers for high-frequency high-power converters,” Ph.D. dissertation, Virginia Polytech. Inst. State Univ., Blacksburg, VA, Jul. 2006.

[38] C. R. Sullivan, “Computationally efficient winding loss calculation with multiple windings, arbitrary waveforms, and two-dimensional or three-dimensional field geometry,” *IEEE Trans. Power Electron.* vol. 16, no. 1, pp. 142-150, Jan 2001

[39] R. P. Wojda and M. K. Kaizimierczuk, “Winding resistance of litz-wire and multi-strand inductors,” *IET Power Electron*., vol. 5, no. 2, pp. 257–268, Feb. 2012

[40] P.L. Dowell, “Effects of eddy currents in transformer windings,” *in Proc. IEE,* Vol.113, pp.1387-1394, Aug. 1966

[41] S. Purushothaman and F. de Leon, “Heat-Transfer Model for Toroidal Transformers,” *IEEE Trans. Power Delivery*, vol. 27, no. 2, pp. 813-820, April 2012.

[42] S. V. Kulkarni and S. A. Khaparde, Transformer Engineering Design & Practice. New York, NY, USA: Marcel Dekker, 2004.

[43] M. Amrhein and P. T. Krein, “3-D magnetic equivalent circuit framework for modeling electromechanical devices,” IEEE Trans. Energy Convers., vol. 24, no. 2, pp. 397–405, Jun. 2009.

[44] J. A. Ferreira, “A Analytical computation of AC resistance of round and rectangular Litz wire windings,” *IEE Proc. B-Elect. Power Appl.,* vol.139, no. 1, pp. 21–25, Jan. 1992.

[45] R. Wrobel and P. H. Mellor, “Thermal design of high-energy-density wound components,” *IEEE Trans. Ind. Electron.*, vol.58, no.9, pp.4096– 4104, Sep. 2011.

[46] R. Wrobel, A. Mlot, and P. H. Mellor, “Contribution of end-winding proximity losses to temperature variation in electromagnetic devices,” *IEEE Trans. Ind. Electron.*, vol. 59, no. 2, pp. 848–857, Feb. 2012.

[47] Jafari, M., Malekjamshidi, Z. and Zhu, J. 2019, ‘Design and Development of a Multi-Winding High-Frequency Magnetic Link for Grid Integration of Residential Renewable Energy Systems', *Applied Energy*, 242, pp. 1209-1225.

[48] J. G. Hayes, D. Cashman, M. G. Egan, and T. O’Donnell, “Comparison of test methods for characterization of high-leakage two-winding transformers,” *IEEE Trans. Ind. Appl.* vol. 45, no. 5, pp. 1729—1741, Sep./Oct. 2009.

[49] H. Akagi, T. Yamagishi, N. M. L. Tan, S. Kinouchi, Y. Miyazaki and M. Koyama, "Power-Loss Breakdown of a 750-V 100-kW 20-kHz Bidirectional Isolated DC–DC Converter Using SiC-MOSFET/SBD Dual Modules," in *IEEE Transactions on Industry Applications*, vol. 51, no. 1, pp. 420-428, Jan.-Feb. 2015, doi: 10.1109/TIA.2014.2331426.

Mohammad Jafari (M’12–SM’19) received the B.E. degree in electrical engineering from Shiraz University, Shiraz, Iran, in 1998, the M.E. degree in electrical engineering from Guilan University, Rasht, Iran, in 2001, and the Ph.D. degree in electrical engineering from the University of Technology Sydney (UTS), Sydney, Australia, in 2017. He has been working on several power electronics projects as a senior design engineer and academician, since 2002. He has authored or coauthored more than 70 peer-reviewed journal and conference papers and several book chapters and received best paper awards in several confrences. His current research interests include power electronic converters, high-frequency transformers and magnetic materials, switching mode power supplies, renewable energy systems, and smart micro-grids.

Zahra Malekjamshidi (S'13–M'19) received the B.E. and M.E. degrees in electrical engineering from Shiraz University, Shiraz, Iran, in 1998 and 2001, respectively, and the Ph.D. degree from the University of Technology Sydney (UTS), Sydney, Australia, in 2018. From 2002 to 2012, she was a research engineer in industries and contributed to the design and development power electronic projects. Her current research interests include matrix converters, dc–dc converters, renewable energy technologies, and smart micro-grids.

Md. Rabiul Islam received the Ph.D. degree from University of Technology Sydney (UTS), Sydney, Australia, in 2014 in electrical engineering.

He was appointed a lecturer at RUET in 2005 and promoted to full professor in 2017. In early 2018, he joined at the School of Electrical, Computer, and Telecommunications Engineering (SECTE), University of Wollongong (UOW), Wollongong, Australia. He is a Senior Member of IEEE. His research interests are in the fields of power electronic converters, renewable energy technologies, power quality, electrical machines, electric vehicles, and smart grid. He has authored or co-authored more than 170 papers including 50 IEEE Transactions/IEEE Journal papers. He has written or edited 4 technical books published by Springer. He has served as a Guest Editor for *IEEE Transactions on Energy Conversion*, *IEEE Transactions on Applied superconductivity* and *IET Electric Power Applications*. Currently he has been serving as an Editor for *IEEE Transactions on Energy Conversion* and *IEEE Power Engineering Letters*, and Associate Editor for *IEEE Access*. He has received several funding from Government and Industries including Australian Government ARC Discovery Project 2020 entitled "A Next Generation Smart Solid-State Transformer for Power Grid Applications".